Characterization of saturated MHD instabilities through 2D electron temperature profile reconstruction from 1D ECE measurements

M Sertoli[1], L Horváth[2], G I Pokol[2], V Igochine[1], L Barrera[1], and the ASDEX Upgrade Team

[1] Max-Planck-Institut für Plasmaphysik, EURATOM Association, Garching, Germany

[2] Department of Nuclear Techniques, Budapest University of Technology and Economy, EURATOM Association, Budapest, Hungary

E-mail: marco.sertoli@ipp.mpg.de

Abstract. A new method for the reconstruction of 2D electron temperature profiles in the presence of saturated MHD modes from the 1D ECE diagnostic is presented. The analysis relies on harmonic decomposition of the electron temperature oscillations through short time Fourier transforms and requires rigid poloidal mode rotation as only assumption. The method is applicable to any magnetic perturbation as long as the poloidal and toroidal mode numbers m and n are known. Its application to the case of a $(m, n) = (1, 1)$ internal kink mode on ASDEX Upgrade is presented and a new way to estimate the mode displacement is explained. For such modes, it is shown that the higher order harmonics usually visible in the ECE spectrogram arise also for pure $m = n = 1$ mode and that they cannot be directly associated to $m = n > 1$ magnetic perturbations. This method opens up new possibilities for electron heat transport studies in the presence of saturated MHD modes and a way to disentangle the impurity density contributions from electron temperature effects in the analysis of the SXR data.

PACS numbers: 52.25.Os, 52.25.Xz, 52.30.Cv, 52.50.Sw, 52.55.Fa, 52.55.Tn, 52.70.Ds, 52.70.Gw

Keywords: tokamaks, ECE, magnetic measurements, MHD instabilities, internal kink, sawtooth, mode displacement, Fourier transform, ECR heating, data analysis

1. Introduction

The experimental characterization of magneto-hydro-dynamic (MHD) instabilities in the core of tokamak plasmas usually requires complex simulation and data analysis tools. Of the various diagnostics available in modern tokamaks, magnetic pick-up coils, soft X-ray diode (SXR) detector arrays and the electron cyclotron emission (ECE) diagnostic are the most used. Each of these diagnostics measures different properties of the plasma in different ways and deliver different information on the MHD instabilities, each with its own advantages and disadvantages. Magnetic coils measure the magnetic field perturbation at the plasma edge, so they are often not suited for core MHD studies because of phase-folding problems with modes located at the plasma edge [1]. SXR diodes are line-of-sight (LOS) integrated measurements of the plasma emissivity in the soft X-ray range so can efficiently detect the core

perturbations, but the integration along the LOS leads to higher harmonic oscillations not directly related to higher harmonics modes in the plasma core [2]. The ECE diagnostic [3] measures the electron temperature locally at different radii along the plasma cross-section usually spanning the full minor radius, but its 1-dimensional measurement can't directly deliver global quantities of the studied instability. Recent upgrades of this diagnostic to 2D imaging [4] have lead to powerful enhancements of its capabilities, but, despite the most recent developments comprising of both low-field-side (LFS) and high-field-side (HFS) detectors so to simultaneously measure on both sides of the magnetic axis [5], it is still limited in radial coverage, spanning only fractions of the minor radius.

In this paper, a new way to reconstruct 2-dimensional electron temperature profiles on the full poloidal plane from the standard 1D ECE diagnostic is explained. The method is applicable in cases in which the mode rotates rigidly and if the growth rate of the instability is much smaller than the angular frequency of rotation of the mode ($\gamma << \omega$). A similar analysis has been performed in the past on TFTR with an ECE diagnostic having channels on both HFS and LFS, re-mapping the measured signals on the poloidal plane through interpolation of subsequent time-points during the rotation of the mode [6, 7] and the same method has been more recently applied for the characterization of electron density profiles (from reflectometry) in sawtoothing plasmas on Tore Supra [8]. The new method presented in this paper relies instead on reconstruction of the measured data from its frequency components characterized through short time Fourier transform (STFT). In comparison to the analysis developed on TFTR, this method is less prone to experimental errors since it naturally filters out the noise in the measured signals which could strongly affect the interpolation. Even for low intensity signals, very precise reconstructions can be performed. The radially resolved amplitude and phase information of the oscillations furthermore enables the reconstruction of the 2D profiles in any mode phase instead of being restricted to the time-point under consideration. Since a few oscillation periods are needed to characterize the perturbation, the time resolution is slightly lower than the TFTR method.

The results obtained can be used for the characterization of magnetic perturbation for any given (m, n) mode numbers and for the investigation of 2D electron heat transport in the presence of saturated modes and of external sources. For $(m, n) = (1, 1)$ MHD perturbations, the resulting 2D profiles can be further used to evaluate the mode displacement. This task is usually complex and requires intensive modeling, while the present method evaluates the displacement from the experimental data directly through a simple geometrical analysis of the 2D temperature contours

Moreover, the reconstruction of mode-resolved electron temperature profiles gives the possibility of disentangling the impurity density and electron temperature contributions from the analysis of the data of the soft X-ray diode (SXR) diagnostic. This can then give the chance to investigate the mode-resolved impurity density profiles instead of analysing only the SXR emissivity profiles obtained by tomographic inversions.

The quality of the reconstruction method has been tested for many different cases and has been found to be reproducible. In this paper, an example of a $(m, n) = (1, 1)$ mode is used to describe the analysis method (section 2), to explain the reconstruction of the 2D electron temperature profiles at any given mode phase (section 3) and the evaluation of the mode displacement (section 4). In section 3 it will be also shown how higher order harmonics in the ECE signals do not necessarily imply higher harmonic

components in the magnetic perturbation but are a direct consequence of the ECE measurement. Conclusions and an outlook on future applications are given in section 5.

2. Analysis principles

Any periodic signal can be decomposed into the sum of a constant (representing its offset) and of harmonic components whose amplitude and phase can be calculated through the use of Fourier transforms. If more than one data-set made up of the same frequency components is analyzed, the phase shift between these sets, the cross-phase, can also be evaluated. These four quantities (average value, amplitude, phase and cross-phase of its frequency components) make up a complete set of variables through which the data-sets can be fully reconstructed.

For the specific case of the reconstruction of ECE electron temperature data, ASDEX Upgrade discharge # 25091 will be used as example. This is a low current $I_p = 0.6\ MA$ (figure 1a), low line-averaged density $\langle n_e \rangle \sim 2. \cdot 10^{19}\ m^{-2}$ (1b), diverted plasma discharge, whose flat-top geometry is shown in figure 3(c). Successive 100 ms on-off cycles of 1.5 MW ECRH power injection (1d) have been performed, depositing the power on a flux surface at $\sim 8\ cm$ from the magnetic axis. The effect of ECRH is clearly visible in T_e as diagnosed from the most central channel of the ECE diagnostic (1c) which exhibits an increase of up to a factor 2 with respect to the ohmic phases. Strong oscillations caused by a $(m, n) = (1, 1)$ mode are also visible in the T_e time trace during ECRH injection, with sawtooth crashes ($\tau_{ST} \sim 40\ ms$) routinely interrupting the cycles. One of these cycles (in time range $[t_0, t_2]$ defined in figure 1) is shown in figure 2 as diagnosed by two ECE channels at $\langle r \rangle \sim 6\ cm$ (a) and 12 cm (b), where $\langle r \rangle = (R_{LFS} - R_{HFS})/2$ is the LFS-HFS averaged equilibrium minor radius at the midplane. Their spectrograms (figures 2c and 2d) reveal various frequency components, not equally intense at different radii, appearing very early in the ST-cycle ($\tau_{ST}/10$) and fully saturated for more than half of it.

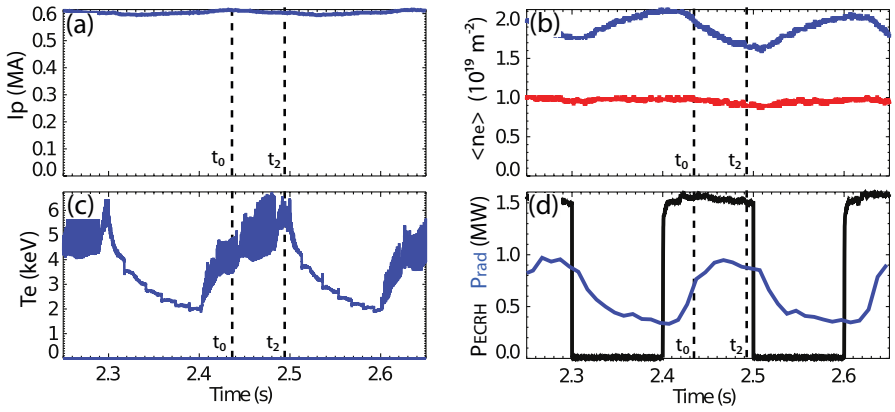

Figure 1. Plasma parameters of AUG discharge # 25091: (a) plasma current, (b) core (blue) and edge (red) LOS-integrated electron density, (c) most central electron temperature measurement from ECE, (d) external ECRH heating power (black) and total radiated power (blue).

2.1. Fourier transform analysis

The spectrograms in figure 2 show the energy density E_d evaluated through the use of continuous short time Fourier transforms [9] (STFT) using a Gaussian window function (Gabor atom), implemented in custom IDL routine [10] †:

$$E_d(t', \omega) = \left| \int_{-\infty}^{\infty} T_e(t)\, e^{-\jmath\omega t}\, g(t - t')\, dt \right|^2 \tag{1}$$

where $g(t - t')$ is the Gaussian function centered on t'. In order to apply a continuous transform on discrete time signals, the transform has to be discretized. This is achieved by replacing the integrals by sums and discretizing all variables with the smallest possible steps, in the present case equal to $dt \sim 0.26\ ms$ (equivalent to 8 data-points). The Gabor atom used has a sigma of 16 data points ($\sigma_t \sim 0.5\ ms$) which determines the time-frequency resolution of the transform. Since the atom has an infinite support it has to be truncated. To preserve the appealing properties of the continuous transform, only the part where its values are under a few orders of magnitude of the maximum is neglected. In figure 2 the truncation is done for 20 σ_t, leading to a frequency step $df \sim 49\ Hz$. The maximum frequency displayed in the figure is the Nyquist frequency of the ECE acquisition system $f_{Ny} = 15.625\ kHz$ (ECE sampling frequency $f_S = 31.25\ kHz$). The parameters of the STFT (window width, time and frequency resolution) can be varied according to the process under investigation.

† NTI Wavelet Tools, Institute of Nuclear Techniques (NTI) Budapest University of Technology and Economics, `https://deep.reak.bme.hu/projects/wavelet`

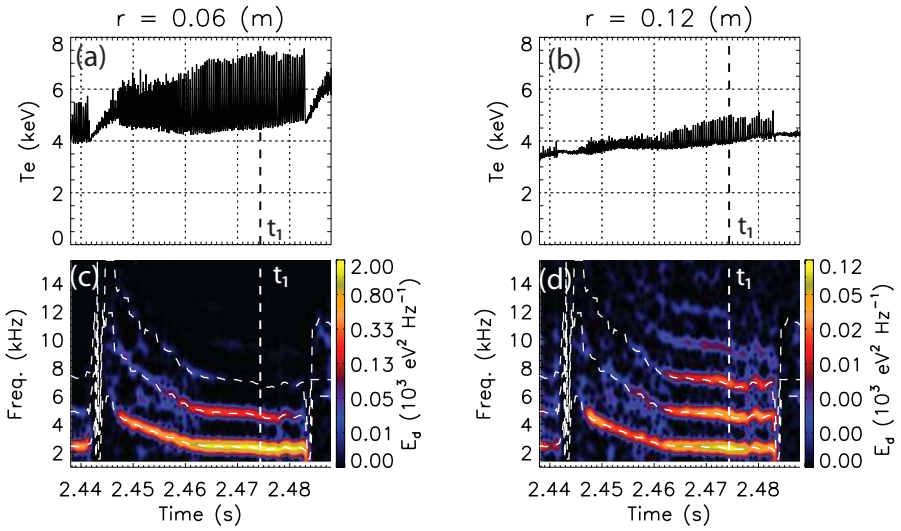

Figure 2. Time evolution of two ECE channels at 6 *cm* (a) and 12 *cm* (b) from the magnetic axis in the time range $[t_0, t_2]$ defined in figure 1. Energy density of their STFT ((c) and (d) respectively) performed with the parameters defined in the text. Dashed white horizontal lines are the result of the maximum-search algorithm returning oscillation frequency and amplitude of the first three frequency components.

Since the window function used for the STFT is a Gaussian and its Fourier transform is still a Gaussian, the energy density at the oscillation frequency will be spread out on the frequency axis following a Gaussian curve whose sigma can be evaluated from the σ_t[10]:

$$\sigma_f = \frac{1}{2\pi\sigma_t} \tag{2}$$

Recovering the maximum in energy density for each frequency component through a maximum-search algorithm, the amplitude in eV can be evaluated using the analytical formula for the integral of a Gaussian, remembering that the energy density (equation 1) is the absolute-value-squared of the Fourier transform [10]:

$$A = \sqrt{\frac{2E_{peak}\sigma_f\sqrt{\pi}dt}{T}} = \sqrt{2E_{peak}\sigma_f\sqrt{\pi}} \tag{3}$$

where E_{peak} is the peak energy density at the oscillation frequency and T is the investigated time interval, in this specific case coinciding with the spectrogram time step dt.

Performing this for each ECE channel and evaluating the cross-phase of each channel with respect to a chosen reference, the electron temperature oscillations of all channels are completely characterized with respect to each other for all radial measurements and for each time-point of the spectrogram. The amplitude and cosine

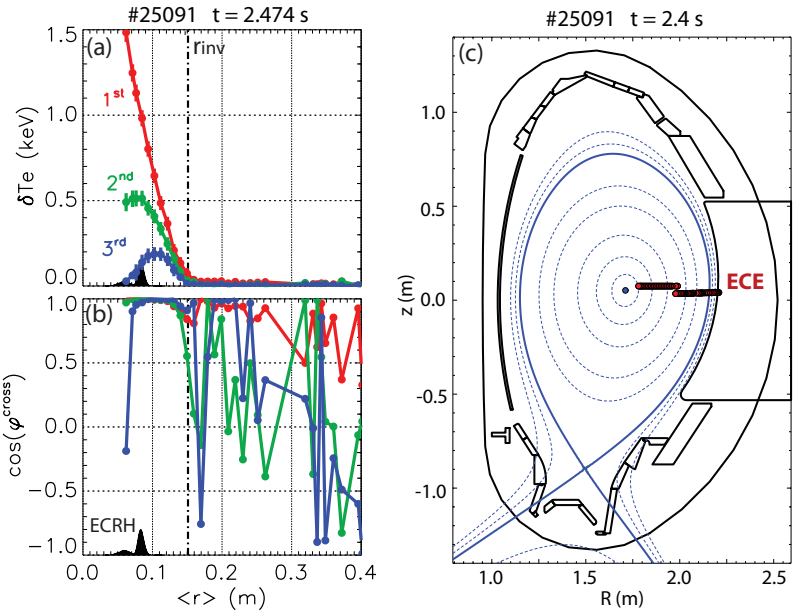

Figure 3. T_e oscillation amplitude (a) and cosine of the cross-phase (b) of the first three frequency components (red, green and blue respectively) at 2.474 s (labelled t_1 in figure 2) for all ECE channels inside $r < 0.4$ m: vertical dashed line is the approximate position of the inversion radius, the black Gaussian curves the ECRH deposition position. Plasma poloidal cross-section (c) at 2.4 seconds and measurement positions of the ECE diagnostic (red dots).

of the cross-phase of the three frequency components of all available channels inside $\langle r \rangle < 0.4\ m$ at time $t_1 = 2.474\ s$ (as defined in figure 2) are shown in figure 3a and 3b respectively. By plotting $cos(\varphi_{cross})$, all channels with the same phase of the reference will be equal to 1, while a value of -1 will correspond to a phase jump of π. Details on the evaluation of the *cross-phase* will be given in the next section.

The error bars on the amplitude have been evaluated through Gaussian propagation of the errors on the measured signals [10], assumed to be $\sim 7\%$ of the measured values. The dashed-dotted vertical line in 3a and 3b shows the position of the inversion radius ($r_{inv} \sim 0.15\ m$), defined as the position where, at the crash time, for $r < r_{inv}$ the temperature drops while for $r > r_{inv}$ it rises. The black Gaussians the ECRH deposition position evaluated through the TORBEAM code [11]. Figure 3c shows the plasma geometry from the *EQI* equilibrium reconstruction [12] and the ECE measurement positions (red dots).

Since the maximum-search algorithm mentioned above returns amplitudes and frequencies for each channel independently, a consistency check of the mode frequency along the minor radius can be performed. Evaluating the mean $\langle f_1 \rangle$ and standard deviation σ_{f_1} of the first harmonic frequency for all time-points analysed and considering all channels inside the inversion radius $r < r_{inv}$ (eleven altogether), the deviation is found to be $\sigma_{f_1} < 1\%\ \langle f_1 \rangle$ for $2.446 < t < 2.481\ (s)$, i.e. for the full time range of mode existence (see figure 2).

2.2. Signal reconstruction in time

The reconstruction of the data of any channel in time is now straightforward. Since 95% of the signal energy of the Gaussian is concentrated in a $4\ \sigma_t$ interval, the data represented by the STFT at any time point t is contained in a time window $4\ \sigma_t$ wide and centered on t. This data-set (black points with error bars figure 4a and 4b) can be reconstructed through its frequency components via the formula:

$$T_e(t) \ = \ \langle T_e(t) \rangle + \sum_{k=1}^{N} \delta T_e(k) \cdot cos(\omega_k t + \varphi_k) \tag{4}$$

where t is the time and $\langle T_e \rangle$ is the average value over the time-window $4\,\sigma_t$ wide centered on t; $\delta T_e(k)$, φ_k and ω_k are the amplitude, phase and frequency of component k respectively, and the sum is performed over all relevant frequency components. In this case only the first three harmonics are considered ($N = 3$) since for $N > 3$ (4^{th} harmonic visible in the spectrogram of the channel at $12\,cm$ in figure 2d) the amplitudes are low enough to be neglected. The frequencies ω_k have been recovered through the maximum-search algorithm used to find the maximum in energy density. If the higher components are harmonics of the first one, as is the case of the present example, then $\omega_k = k \cdot \omega_1$, where ω_1 is the oscillation frequency of the 1^{st} harmonic. In order to guarantee a precise phase evaluation, φ_k is not taken from the result of the STFT, but is evaluated as a cross-phase with respect to a simulated reference signal oscillating at the same frequency ω_k. Since this reference is chosen with zero phase, the resulting cross-phase will be exactly φ_k.

Using equation 4 with all three frequency components and the parameters as described above, the reconstruction shown in figure 4a and 4b as a thick red line overlapping the data is obtained. Its precision in both frequency and amplitude, visible at first sight, can be mathematically quantified by evaluating the residuals $r = (data \ - \ fit)/error$ (where fit is the reconstructed signal) whose absolute

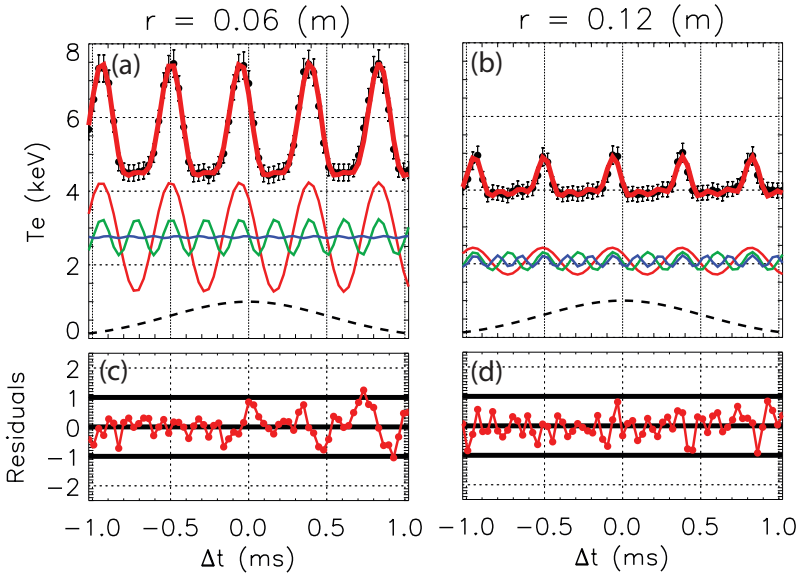

Figure 4. Reconstruction of the ECE data (black with error bars) using all three frequency components (thick red line is the sum of all components) at time t_1 as labeled in figure 2. Light red, green and blue lines in (a) and (b) show the 1^{st}, 2^{nd} and 3^{rd} components respectively shifted in absolute value for best visualization. Dashed black curve at the bottom of (a) and (b) is the Gaussian curve used for the STFT. (c) and (d) show the residuals of the reconstruction of (a) and (b) respectively.

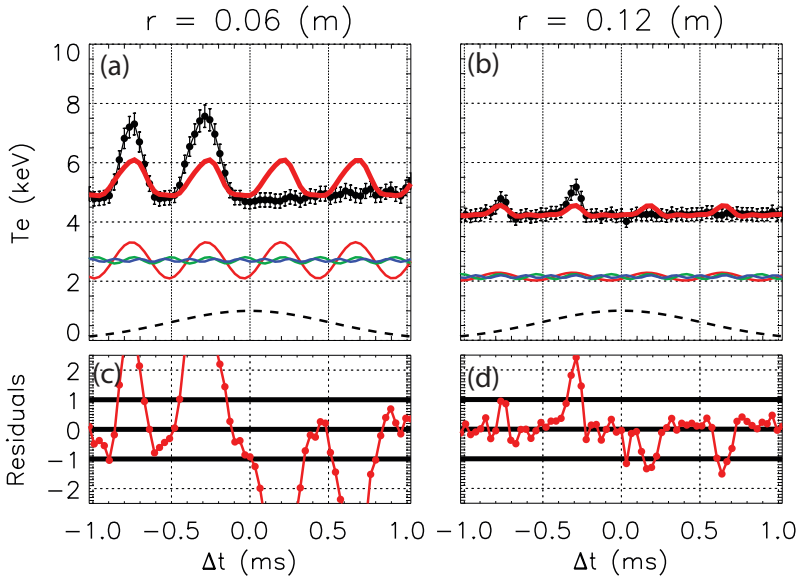

Figure 5. As in figure 4 but for the last time-point previous to the sawtooth crash at $t \sim 2.483\ s$.

values always remain below 1 for both considered channels and for the full time range (the same is found for the full radial range). Analysing the residual distribution from a statistical point of view, if the ECE data is distributed following the normal distribution then error in the formula of the residuals corresponds to the standard deviation σ. For such a distribution one would expect $\sim 68\%$ of all the data to fall within $|r| \leq 1$, $\sim 95\%$ within $|r| \leq 2$. Fitting a gaussian to the residual distribution function, one obtains a standard deviation of ~ 0.25. One can therefore conclude that the errors on the ECE data are slightly overestimated, the statistical error on the ECE data being of the order of 2% instead of the 7% assumed. The matching between the reconstruction and the data can anyway be considered of very high accuracy.

As can be seen from the single frequency components plotted as narrow red, green and blue lines respectively (slightly shifted in absolute value for best visualization), the three components are found to be *phase-locked* with each other, so that maxima in the first harmonic correspond to maxima in both second and third harmonics. This well defined phase relation between the different harmonic components will enable us to discard the phase φ_k of each component in the reconstruction of the profiles and use only the cross-phase between channels as phase information.

For completeness, the reconstruction at the crash time is shown in figure 5. As explained in the previous paragraphs, since the rate of change of the electron temperature oscillation is in this case much faster than the angular frequency of the mode and therefore much higher than the time resolution of the STFT, the reconstruction clearly fails (see residuals in figure 5c and 5d). In this specific case, the mode frequency is so low ($\sim 2\ kHz$) that, as a result of the crash, the amplitude goes to zero within a fraction of the mode rotation, making it impossible to resolve the crash phase even through the use of the method developed at TFTR [6, 7] would give the possibility of resolving the crash phase.

3. 2D profiles

Having demonstrated the high quality of the reconstruction in time, the second step is to reconstruct the profiles at the different phases of the mode rotation. In this case, the formula is similar to equation 4, but now includes only a phase term φ^{rm} remapped to $\vartheta = 0$ and a term dependent on the poloidal angle ϑ:

$$T_e(r, \vartheta) \;=\; \langle T_e(r, t) \rangle +$$

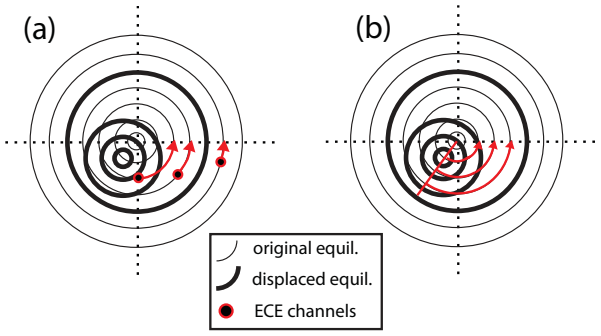

Figure 6. Correction of geometrical phase shifts of the ECE channels (a) and of the mode phase to $\vartheta = 0$.

$$\sum_{k=1}^{N} \delta T_{e,k}(r) \cdot cos[m_k\,\vartheta + \varphi_k^{cross}(r)] \tag{5}$$

The average $\langle T_e(r,t)\rangle$ is performed over time as in equation 4, independently for each radial channel, and the radial coordinate r is the distance of the ECE channel from the original magnetic axis. Since the measurement is performed only on the LFS, the reconstruction is performed assuming that the measurements are representative of the electron temperature on the full poloidal plane. The poloidal angle term includes the poloidal mode-number m_k and no toroidal angle information is needed since the toroidal position of all ECE channels is the same. Also the time-frequency term ωt is neglected since we are not interested in knowing the exact phase of the mode in front of the ECE diagnostic, but want to reconstruct the electron temperature profile at any phase of the mode. This will in the future give the possibility to reconstruct the 2D profiles at the phase of measurement from any other diagnostic on the tokamak.

Since the ECE channels measure at different poloidal angles (e.g. the black dots in figure 6a), this will lead to phase shifts between the channels due solely to the measurement geometry. The phase φ_k of each channel and of each frequency component as evaluated in the previous section is corrected for such shifts by remapping each channel to the LFS mid-plane (figure 6a), where the poloidal angle is equal to $\vartheta = 0$ following the AUG convention, with ϑ increasing positively in the counter-clockwise direction:

$$\varphi_k^{rm}(r) = \varphi_k(r) - m_k \vartheta_r \tag{6}$$

where ϑ_r is the poloidal angle of the ECE channel at position r from the plasma centre. If the temperature profile is peaked in the centre (as it almost always is), the remapped phase of the first frequency component $\varphi_1^{rm}(r)$ from equation 6 is also the phase of the mode in the laboratory frame at the toroidal position of the ECE antenna. Since our aim is to reconstruct the mode at any given phase, after the geometrical correction performed through equation 6, the phase is further remapped as if the mode were at $\vartheta = 0$ (figure 6b):

$$\begin{aligned} \varphi_k^{cross}(r) &= \varphi_k^{rm}(r) - \frac{\omega_k}{\omega_1}\,\varphi_1^{rm}(r_{ref}) \\ &= \varphi_k^{rm}(r) - n\,\varphi_1^{rm}(r_{ref}) \end{aligned} \tag{7}$$

where ω_k/ω_1 accounts for the periodicity of the higher harmonics components, and n is the toroidal mode number. This remapping guarantees that any phase shift between single channels and between harmonic components remain unaltered. This is therefore a *cross-phase* not only between channels at the same frequency, but also a *cross-phase* between frequency components. The result of equation 7 is the phase used for the profile reconstruction.

Finally, the mapping on the poloidal plane along ϑ in equation 5 is performed along the surfaces of the original magnetic equilibrium since these are the trajectories of rotation of displaced fluid elements. The reconstruction is performed assuming rigid poloidal mode rotation, i.e. on the geometrical ϑ. A discussion of the consequence of this assumption is given at the end of this section where the rigidity condition is relaxed and the reconstruction is performed on the straight field angle ϑ^* as poloidal coordinate [13].

3.1. Higher order δT_e harmonics

It is clear from equations 5 and 6 that in order to reconstruct the 2D electron temperature profiles, the poloidal mode numbers must be known. By performing mode-number analysis on the magnetic coils and SXR diodes, the first frequency component has been found to be a $(m, n) = (1, 1)$ mode. Comparing the spectrogram of one ballooning coil ($B31-12$) which measures the radial component of the magnetic perturbation, with that of the ECE channel at $r \sim 12$ *cm*, the higher frequency components visible in the ECE spectrogram (figure 7a) are not visible in that of the coil (figure 7b). While the amplitudes of the 2^{nd} and 3^{rd} harmonic in the two ECE channels considered (figure 7c) are only fractions of the first one, in the magnetic measurement their values are at noise level (figure 7d). Since the higher frequency components in the ECE spectrum are higher harmonics of the first one, at double and three times the main frequency, it could be sensible to assume that the three frequency components are in direct relation to $(m, n) = (1, 1)$, $(2, 2)$ and $(3, 3)$ magnetic perturbations. If this were the case, then an estimate of the mode displacement due to each harmonic could be evaluated through [14]:

$$\xi^{mn} \sim -\frac{\delta T_e^{mn}}{\nabla \langle T_e \rangle} \tag{8}$$

where the gradient is performed on the equilibrium electron temperature. It will be clear in the next paragraphs and in the next section that the higher harmonics in equation 5 should be modeled with $m_k = 2$ and $m_k = 3$, but that they cannot be directly associated with higher order harmonics in the magnetic perturbation since they can arise even from a pure $(m, n) = (1, 1)$ mode. Let us for the moment assume that equation 8 holds and try to understand the relation between the ECE and magnetic measurements, and higher order displacements in the plasma core.

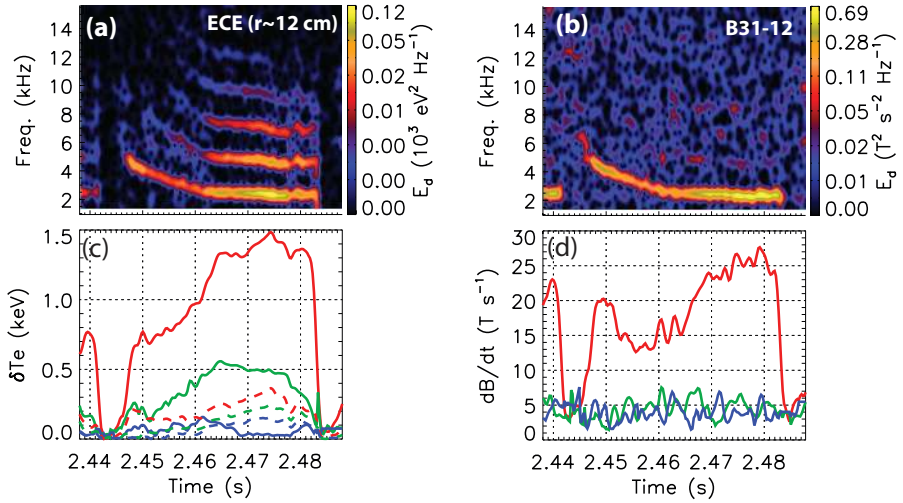

Figure 7. Spectrogram of ECE channel at 12 *cm* from the plasma centre (a) and of the ballooning coil *B31-12* positioned at 56 *cm* from the magnetic axis (b). The time evolution (c) of the 3 harmonics (color code as in 3) for the two ECE channels (full lines 6 *cm*, dashed 12 *cm*) and for the ballooning coil (d).

3.2. Comparison with magnetic measurements

If equation 8 is applicable to the case of an internal kink $(m, n) = (1, 1)$ with higher order harmonics, then an estimate of the radial magnetic field perturbation amplitude at the resonant surface can be calculated from the displacement values through the relation:

$$\tilde{B}^{mn}_{r,s} \propto \frac{2nB_\phi}{R}\,\xi^{mn} \tag{9}$$

where $R = 1.65\ m$ is the plasma major radius, $n = 1$, 2 or 3 the toroidal mode number and $B_\phi = 2.5\ T$ the toroidal equilibrium magnetic field. Equation 9 is obtained by assuming a typical internal kink *top-hat* displacement function with $d\xi/dr = 0$ [15], and solving Maxwell's equation $\tilde{\mathbf{B}}_s = \nabla \times (\xi \times \mathbf{B_0})$ for the perturbed radial magnetic field $\hat{\mathbf{r}}\,\tilde{B}_{r,s}$, where $\mathbf{B_0}$ is the equilibrium magnetic field.

Applying equation 8 at $t = 2.475\ s$, the time where the mode is fully saturated but still far enough from the sawtooth crash time to allow us to trust the harmonic analysis, one obtains a displacement value of 4 *cm* for the $m = 1$ harmonic (table 1, labeled ECE). The higher harmonics, given as ratios with respect to the value of the 1^{st} one, are 1/2 and 1/4 of the ξ^{11}. For comparison, typical values shortly before the sawtooth crash evaluated through modeling of SXR-diode measurements [16] are also given in table 1 (labeled SXR). The values from the two methods are consistent for the 1^{st} harmonic while the 2^{nd} and 3^{rd} harmonics are extremely high for typical sawtooth precursors, respectively 2 and 14 times larger than the typical values just before the crash. The resulting relative magnetic perturbation amplitude at the resonant surface calculated using the displacement in table 1 and equation 9 are given in table 2 for the 2^{nd} and 3^{rd} harmonics.

	ξ^{11} (cm)	ξ^{22}/ξ^{11}	ξ^{33}/ξ^{11}
ECE	4	0.5	0.25
SXR	6	0.25	0.017

Table 1. Displacement of the first three harmonic components of the $m = n = 1$ mode, evaluated using ECE and typical values obtained from modeling of SXR-diode measurements [16]. The $m = 2$ and $m = 3$ are normalized with respect to $m = 1$ value.

	$\tilde{B}^{22}_{r,s}/\tilde{B}^{11}_{r,s}$	$\tilde{B}^{33}_{r,s}/\tilde{B}^{11}_{r,s}$
ECE	1	0.75
SXR	0.5	0.05

Table 2. Magnetic field perturbation amplitudes of the $m = 2$ and $m = 3$ harmonics at the resonant surface normalized to amplitude of the $m = 1$, evaluated using equation 9 with the displacement values in table 1.

The displacements in table 1 derived using SXR are evaluated by modeling the experimental SXR data using an MHD-interpretation code and reconstructing the displacement eigenfunctions [16]. On the other hand, equation 8 has been calculated

for the so-called *outer-region*, i.e. for radii far from the resonance surface [14]. It is therefore clear that the estimates obtained using SXR given in tables 1 and 2 are to be considered more precise than those evaluated using ECE data. Moreover, in the next paragraphs it will be clear that the 2^{nd} and the 3^{rd} harmonics present in the ECE data are not in direct relation to the structure of the magnetic perturbation, but are a consequence of the ECE measurement.

In order to compare the results in table 2 with the coil measurements performed at the plasma edge, the decay of the magnetic perturbation across the plasma has to be evaluated. This can be calculated by solving Maxwell's equation $\nabla \times \tilde{\mathbf{B}} = \mu_0 \tilde{j}\,\hat{\mathbf{b}}$ for the perturbed magnetic field $\tilde{\mathbf{B}}$ assuming the perturbed toroidal current $\tilde{j}\,\hat{\mathbf{b}}$ is negligible outside the resonant surface $r > r_s$ [17]. Writing the perturbed magnetic field in large aspect ratio approximation in the form of the poloidal flux function:

$$\tilde{B}_r = -\frac{1}{rR}\frac{\partial \psi}{\partial \vartheta} \qquad \tilde{B}_\vartheta = \frac{1}{R}\frac{\partial \psi}{\partial r} \tag{10}$$

and assuming a perturbation of the form $e^{\jmath(m\vartheta - n\phi)}$, substituting equations 10 in Ampére's law, one obtains the tearing mode equation for the outer region:

$$\underbrace{\frac{1}{r}\frac{d}{dr}\left[r\frac{d\psi}{dr}\right] - \frac{m^2}{r^2}\psi}_{vacuum} \;=\; \underbrace{\frac{dj_\phi/dr}{\frac{B_\theta}{\mu_0}\left(1-\frac{nq}{m}\right)}\psi}_{plasma} \tag{11}$$

where the left hand side is the vacuum contribution, the right hand side the contribution from the plasma. In vacuum approximation (i.e. setting the right hand side to zero), this equation has an analytical solution $\psi \propto r^{-m}$. The decay of the magnetic field perturbation can then be calculated substituting this solution in equation 10, obtaining:

$$\tilde{B}^{m,n} \propto r^{-(m+1)} \tag{12}$$

where r is the distance from the magnetic axis and m is the poloidal mode number. Since this solution is exact apart from a constant, the decay rate from the resonant surface to the plasma edge can be evaluated analytically:

$$\frac{\tilde{B}^{mn}_s}{\tilde{B}^{mn}} = \left(\frac{r}{r_s}\right)^{(m+1)} \tag{13}$$

The same estimate can be calculated including the plasma contribution by solving equation 11 numerically with the experimental safety factor q and the toroidal current density j_ϕ profiles, and fixing an arbitrary value at the resonant surface as inner boundary condition and imposing $\psi = 0$ at large distances from the resonant surface (in this case at $r = 2\,a$) as outer boundary condition. The safety factor and current density profiles used for the calculation have been cross-checked against a CLISTE equilibrium reconstruction [12, 18].

The decay rates evaluated for $m = n = 1$, 2 and 3 in both vacuum approximation and including the plasma contribution are shown in table 3 (labeled *vacuum* and *plasma* respectively), the resonant surface assumed at the position of the inversion radius $r_s = r_{inv} = 0.15\ m$ and the decay calculated up to the plasma edge $r = 0.5\ m$. The increase in decay rates for higher m numbers is clear already from the vacuum solution 13. The decay rates increase including the plasma contribution, this increase

	$\tilde{B}^{11}_{r,s}/\tilde{B}^{11}_{r}$	$\tilde{B}^{22}_{r,s}/\tilde{B}^{22}_{r}$	$\tilde{B}^{33}_{r,s}/\tilde{B}^{33}_{r}$
vacuum	11	37	123
plasma	24	50	152
plasma/vacuum	2.18	1.35	1.24

Table 3. Decay rates of the first three harmonic components of the $m = 1$ mode evaluated in vacuum approximation and including the plasma contribution. The last line shows the ratios between these decay rates.

being lower for higher harmonics, the ratio of the decay rates ($plasma/vacuum$) decreasing with m.

Since the magnetic coils measure the rate of change in magnetic field perturbation $d\tilde{B}^{mn}_r/dt$ and not the perturbation amplitude directly, the $\tilde{B}^{mn}_r$ at the measurement position has to be calculated from:

$$\tilde{B}^{mn}_r = \frac{d\tilde{B}^{mn}_r}{dt}\frac{1}{2\pi f_{lab}} = \frac{d\tilde{B}^{mn}_r}{dt}\frac{1}{n\omega_t} \tag{14}$$

where f_{lab} is the measured frequency in the lab frame (different for each harmonic), n the toroidal mode number and $\omega = \omega_t$ the angular frequency of the mode rotation (equal for all harmonics). The latter is assumed to be predominantly in the toroidal direction, neglecting the corrections from the diamagnetic terms and poloidal plasma rotation.

From the measurement value $d\tilde{B}^{11}_r/dt = 25\ T/s$ of the first harmonic at $t = 2.475\ s$ (figure 7), using equation 14 and the decay rate calculated including the plasma contribution, a perturbation amplitude $\tilde{B}^{11}_{r,s} \sim 42\ mT$ is obtained at the resonant surface. Calculating $\tilde{B}^{mn}_{r,s}$ for the higher harmonics using the ratios in table 2 and the decay rates to calculate $\tilde{B}^{mn}_r$, the expected measurement values $d\tilde{B}^{mn}_r/dt$ (table 4, where ∂_t indicates the time derivative) can be estimated using equation 14. The results in table 4 clearly show that both the 2^{nd} and 3^{rd} harmonics should be visible in the magnetic coil measurements, their values being well above the noise level $\sim 5\ (T/s)$. Even using the typical values (SXR), the second harmonics should be visible in the magnetic spectrogram. It is therefore clear that the higher harmonic components in the ECE spectrogram are not in direct relation to the higher harmonics in the magnetic perturbation and that the numbers m_k in equations 5 and 6 can be seen as poloidal mode numbers of the electron temperature perturbation as seen by the ECE diagnostic.

	$\partial_t \tilde{B}^{11}_r$ *meas.* (T/s)	$\partial_t \tilde{B}^{22}_r$ (T/s)	$\partial_t \tilde{B}^{33}_r$ (T/s)
ECE	*25*	24	8.9
SXR	*25*	12	0.9

Table 4. Predicted magnetic measurements evaluated using the decay rates in table 3 and the magnetic perturbation amplitudes in table 2 given the measured value of the $m = 1$ harmonic.

3.3. Profile reconstruction

Let us therefore take $m_k = 1$, 2 and 3 for the three harmonics and rebuild the 2D electron temperature profiles using equation 5 with mode phase $\vartheta = 0$, i.e. with the displaced core on the LFS. All contour plots in figure 8 show only the most central part of the plasma, inside a radius slightly larger than the inversion radius r_{inv} and are truncated for $r < min(r_{ECE})$ so to avoid any extrapolation of the electron temperature to radii where the ECE diagnostic does not measure. Moreover, the re-mapping of the T_e on the poloidal plane is performed on the geometrical poloidal angle ϑ and not on the straight field line angle ϑ^* [13] since, due to the absence of data from the motional Stark effect diagnostic (MSE), a trustworthy q profile for its correct evaluation was not available.

If the reconstruction is performed using only the $(1, 1)$ oscillation component summed to the average profile $\langle T_e \rangle$, bean-shaped surfaces are obtained (figure 8a). The $(2, 2)$ component leads to contours which are squeezed on the top and on the bottom (8b), while the $(3, 3)$ produces triangular shaped surfaces (8c). Finally, summing all the harmonic components to the average profile, quasi-circular surfaces eccentric relatively to the magnetic axis as shown in figure 8d are obtained.

Assuming that the electron temperature is still constant on the displaced flux surfaces, the shape of the T_e contours should resemble that of the magnetic flux surfaces. If the frequency components in the ECE measurement were in direct relation with the harmonic components of the magnetic perturbation, then the $m_k = 1$ in δT_e should resemble the geometry of an $m = n = 1$ mode. As shown in figure 8a this is not

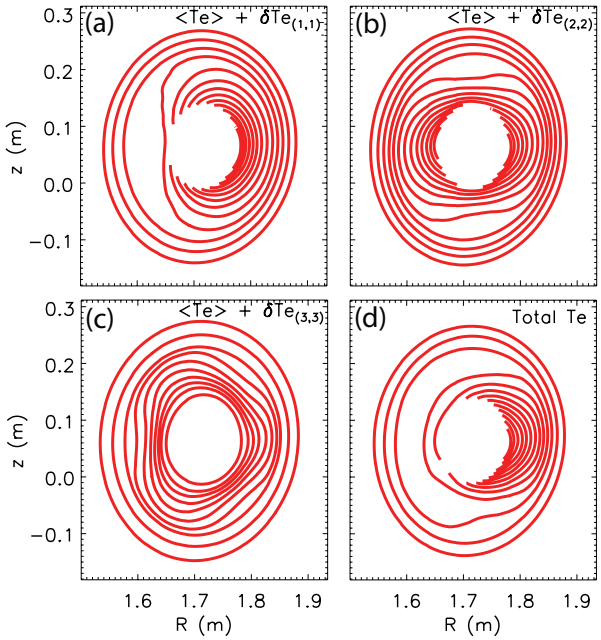

Figure 8. 2D reconstruction of the electron temperature profiles: (a) contours of the electron temperature considering only the $(1, 1)$ oscillation amplitude summed to the average $\langle T_e \rangle$; (b) using only the $(2, 2)$ and (c) only the $(3, 3)$; (d) considering all 3 harmonic components.

the case, and the contours, obtained using the first harmonic only, exhibit a bean-like shape. In previous studies [19], simulations of the electron temperature oscillation in the presence of a resistive $(m, n) = (1, 1)$ mode were observed to exhibit what was then named "frequency doubling" for ECE channels close to the inversion radius. This is an oscillation exhibiting a shape similar to what shown in figure 9d which can be modeled only by including higher harmonics. Since the simulation was performed with no higher harmonics in the magnetic perturbation, it is clear that a $(m, n) = (1, 1)$ perturbation will naturally lead to higher harmonics in the ECE signals, their intensity dependent on the value of the displacement ξ, on the shape of the unperturbed electron temperature profile as well as on the channel under consideration.

A qualitative explanation of this can be provided by following the trajectory of an ECE channel during mode rotation in the mode frame as shown in figure 9a and 9b (mode phase set to $\vartheta = 0$ as in the previous figures). Since the mode rotates rigidly at a constant angular velocity, in the mode frame this is equivalent to consider that each ECE channel will rotate rigidly with constant angular velocity around the equilibrium magnetic axis (black cross) following a trajectory along the unperturbed flux surfaces (blue-black ellipse). If the measured signal were made up of only one frequency, then the T_e contours would be bean-like surfaces (figure 9a) since the positive and negative parts of the oscillation (blue and black parts in figure 9c respectively) account for half of the oscillation period exactly. For the chosen mode phase, the inversion of the oscillation from positive to negative will spatially take place at the axis position,

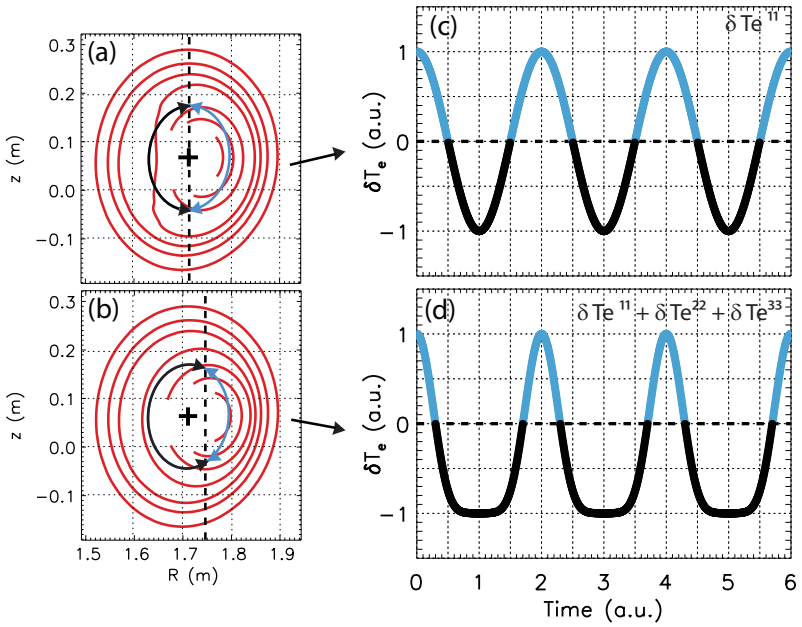

Figure 9. Temperature contours obtained using the $(1, 1)$ δT_e component only for the reconstruction (a) and the contours of an ideal $(m, n) = (1, 1)$ mode (b). Resulting temperature oscillation normalized to range $[-1, 1]$, (c) and (d) for (a) and (b) respectively. Black cross in (a) and (b) is the magnetic axis, the colors of the black-blue ellipse in (a) and (b) correspond to identical phases in (c) and (d).

corresponding to exactly half of the oscillation pertiod (vertical dashed black line in figure 9a). If the geometry of an ideal $(m, n) = (1, 1)$ is considered (figure 9b), the situation changes drastically and the "zero-crossing" is shifted to higher major radii. The ECE channel considered will exhibit a phase where it *sees* a constant temperature (that of the flux surface closest to the measurement position on the left side of the axis in figure 9b) and a flattening will appear on the time signal (as in figure 9d). This signal will naturally exhibit higher harmonics. This explanation, given for an ideal $(m, n) = (1, 1)$ mode, is naturally extendable to a resistive mode with flat electron temperature in the island. In this case, the flattening observed on the electron temperature measurement will coincide with the phase in which the ECE channel measures deep inside the island, as for the results in [19].

It is therefore clear that a one-to-one correspondence between higher order harmonics in the electron temperature perturbation and harmonics in the magnetic perturbation cannot be done. Moreover, since also magnetic measurements cannot provide a trustworthy estimation of the intensity of the harmonics, the identification of higher (m, n) components of the internal kink must be performed in a more indirect manner. A possible solution will be given in the next section.

3.4. Time evolution during a sawtooth cycle

The resulting 2D profiles considering the contribution from all 3 harmonics in the electron temperature oscillation are plotted in figure 11 for four time-points in the sawtooth cycle (defined in figure 10 with the same labeling). All surfaces are plotted with the same color scale and same contours so to show the changes in electron temperature occurring during the cycle. The thick dashed white ellipse represents flux surface of deposition of the ECRH, the full one the position of the inversion radius.

Following the time evolution during the ST-cycle, one can observe how the contours are all concentric surfaces at the time-points where the mode is not yet present or is very low in amplitude (t_0 and t_1). Just before the rise of the perturbation (t_1), the temperature inside the inversion radius has increased, perfectly in line with the fact that the ECRH is being deposited deep inside r_{inv}. At t_2, the displacement of the contours is already clearly visible. Finally, at full saturation of the mode and shortly before the second crash (at t_3), the contours are displaced even further and the higher temperature of the core is now visible. At this stage, it is not clear if the

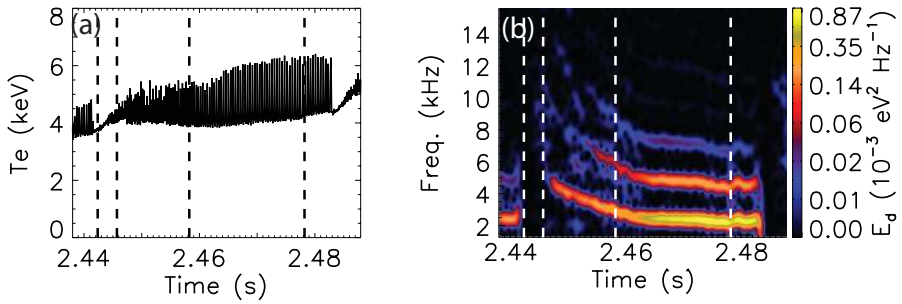

Figure 10. Time evolution (a) and spectrogram (b) of the ECE channel at 6 *cm* from the magnetic axis.

temperature inside the displaced core is still increasing between t_1 and t_3 or if it is simply being further displaced into the region of measurement.

The slight discontinuity in the contour just inside the inversion radius in figure 11 is probably due to the low oscillation amplitude at this radius which leads to errors in the cross-phase between neighboring channels and thus to slight imprecisions in the 2D reconstruction.

To best visualize the time evolution of the electron temperature within this sawtooth cycle, radial cuts of the profiles in figure 11 at the mid-plane are plotted in figure 12. Here, *displaced-core* refers to the right side in the plots in figure 11, *island-side* to the left side where the magnetic island sits if the mode is resistive. As predictable, the T_e profiles (figure 12a and 12b) and their gradients (figure 12c and 12d respectively) at t_0 are symmetric on both sides of the mode, the gradients exhibiting very low values just inside the inversion radius.

As time passes, T_e increases strongly on the side of the displaced core, while the temperature on the *island-side* remains approximately stable. Due to the mode rotation, the ECRH is being deposited equally on both sides of the mode following the dashed white ellipse in figure 11, but only the *displaced-core* seems to retain the deposited heat. The normalized logarithmic gradients show this effect even more clearly, the displaced core exhibiting up to 5 times higher values in comparison to those on the *island-side*. The latter shows a slight evolution only for the first phase

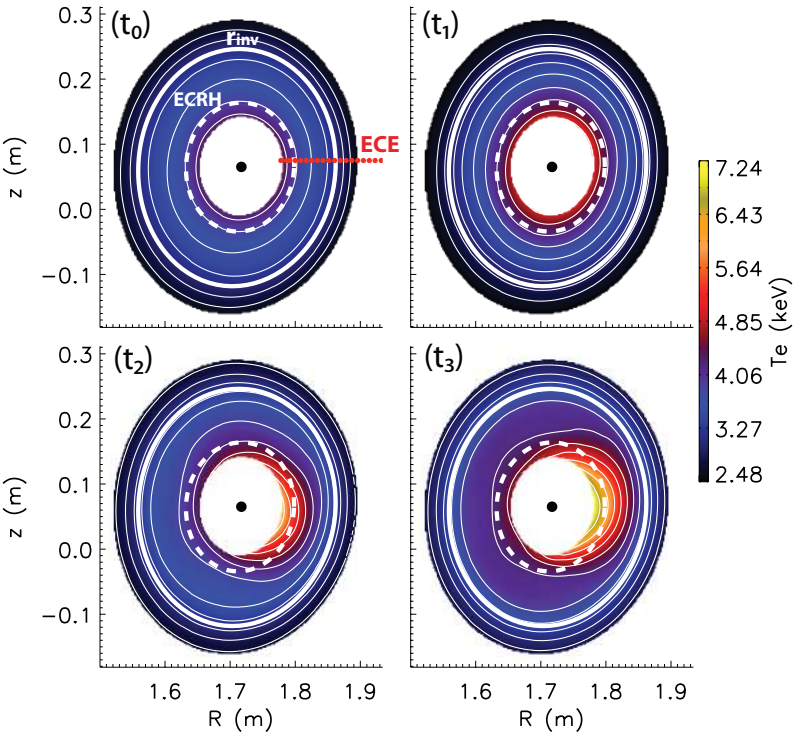

Figure 11. Absolute value of the 2D electron temperature at the time-points defined in figure 10 (same labels). Dashed white ellipse is the position of deposition of the ECRH, full white one that of the inversion radius.

$t_0 \rightarrow t_1$ (black and blue profiles), time at which the mode is starting, visible in the gradients in the two mode phases, differing only for $\langle r \rangle < 0.1\ m$. In the last two time-points (red and orange) the gradients on the *island-side* are instead at the level of the crash value (black) while the ones in the *displaced-core* continue to evolve.

Further interesting information can be obtained by subtracting the average 2D profiles $\langle T_e \rangle$ shortly after the crash (at t_0 in figure 11) from each time-point and plotting the time evolution of the 2D profiles with respect to the start of the sawtooth cycle (figure 13). The profile at t_0 is obviously approximately zero on the full poloidal plane since the subtracted average is that of this time-point. At t_1, the temperature close to the ECRH deposition position has increased by fractions of a keV while the temperature at the inversion radius has not changed and the surfaces are still approximately concentric. The shift of the displaced core is now very clear at t_2 and t_3, showing an increase of the displacement and of the temperature inside the displaced core up to $\sim 3\ keV$ with respect to the start of the sawtooth cycle at t_0. In comparison to the plots of the absolute values (figure 11), it is now clear that between t_1 and t_3 the core is not only being displaced further, but the electron temperature inside it is still increasing. On the *island-side* of the mode, the temperature instead does not increase more than a few percent and is approximately constant across the full region throughout the complete sawtooth cycle, indicating that the mode is most probably of resistive nature and that the temperature inside the island is approximately flat.

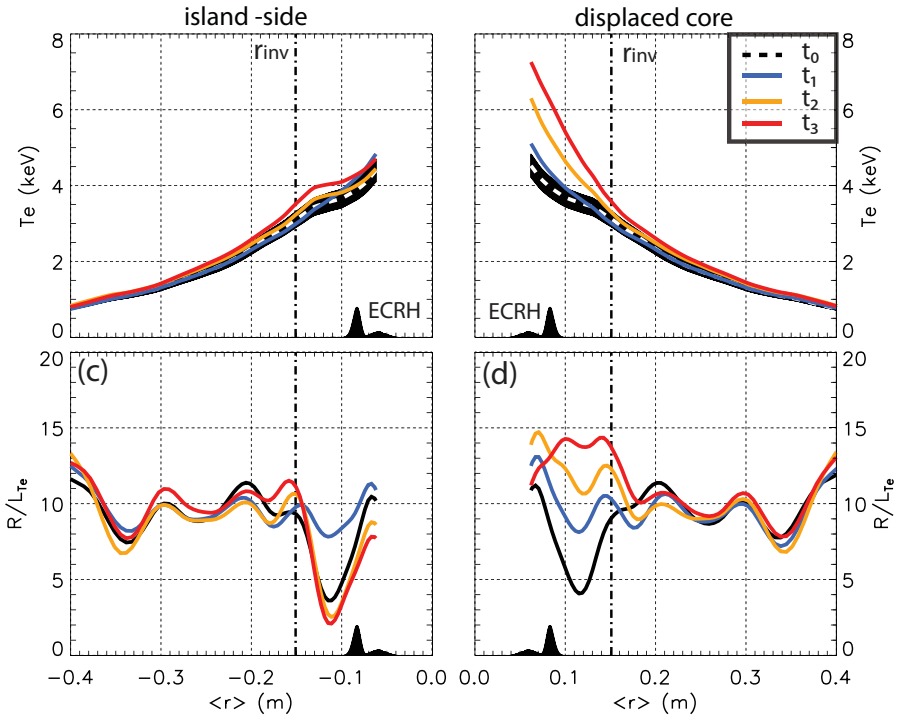

Figure 12. Electron temperature profiles on the *island-side* (a) and *displaced core* side (b) and their normalized logarithmic gradients, (c) and (d) respectively, for the time-points defined in figure 10. The black band of the T_e profiles for t_0 show the error on the electron temperature profiles.

Despite highlighting differently various properties of the mode evolution, both absolute-value and background subtracted 2D profiles show quasi-circular contours in the displaced core. One of the possible reasons for this is that the re-mapping of the profiles to 2D has been performed using the geometrical ϑ and not on the straight field angle ϑ^* as poloidal coordinate [13]. Using the q-profile given by the equilibrium reconstruction the differences between the two poloidal coordinates can be seen in figures 14a and 14c, plotted with the same contour levels for best comparison. Using these coordinates time-point t_3 of the background-subtracted profiles are plotted in figures 14b and 14d for ϑ and ϑ^* respectively. A slightly smaller radial range with respect to what shown in figure 13 has been chosen so to best highlight the contours and surfaces. It is clearly visible that more stretched surfaces arise when using the straight field line angle as poloidal coordinate. With respect to those obtained by mapping on the geometric ϑ, these are more similar to the expected shape of an $(m, n) = (1, 1)$ perturbation in an elongated plasma.

Also the presence of higher order harmonics in the magnetic perturbation could naturally lead the displaced core to exhibit slightly more squeezed surfaces. On the other hand, as explained previously, their presence cannot be determined directly by either magnetic or ECE measurements. A possibility to understand if the mode includes higher order harmonics is to model the magnetic perturbation with higher order displacement vectors (m, n), reconstruct the flux surfaces and try to match the

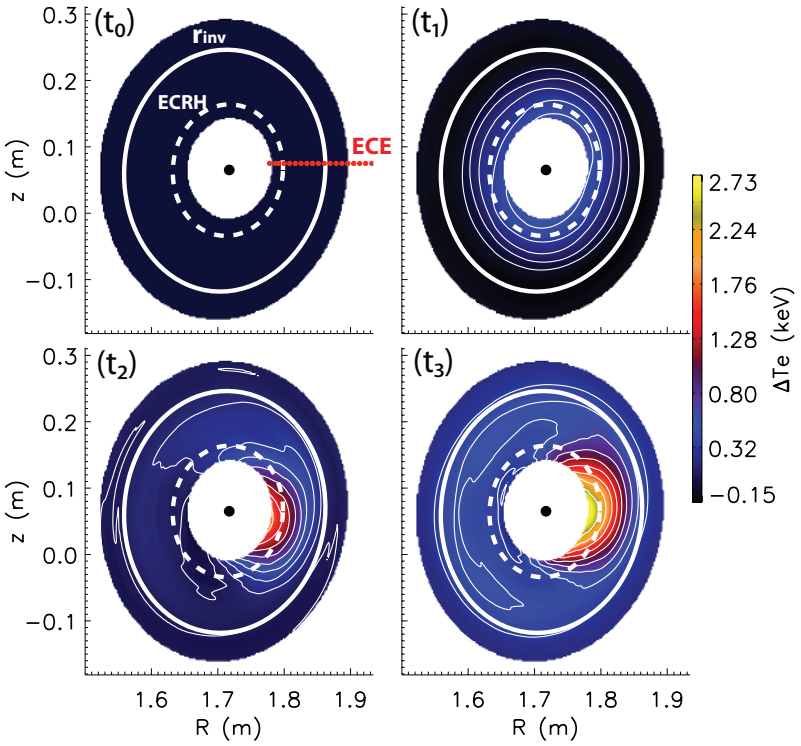

Figure 13. 2D electron temperature profiles background subtracted with respect to the average 2D profile at start of the sawtooth cycle (t_0). Labels as in figure 11.

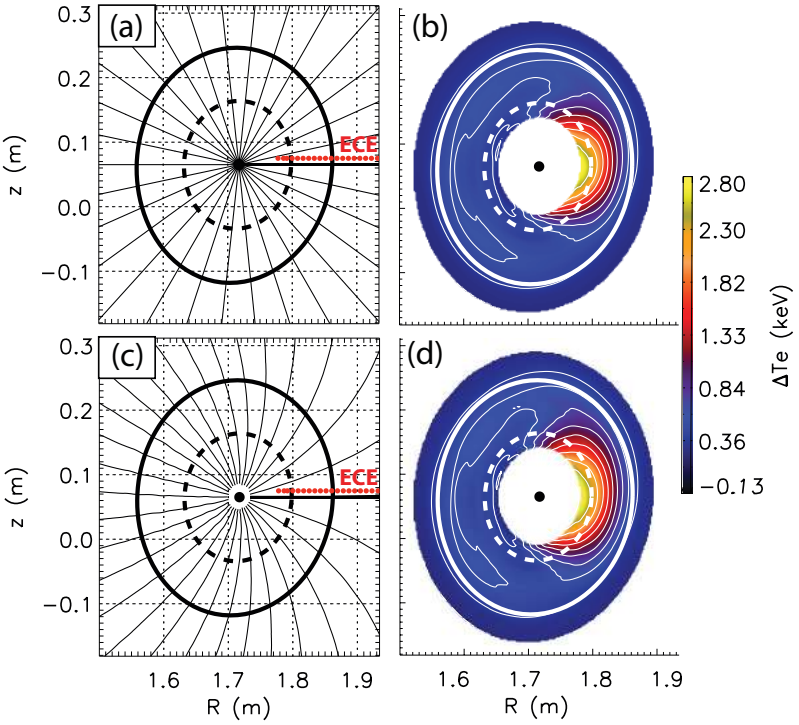

Figure 14. Geometrical (a) and straight filed line poloidal angles (c) used to map of the background subtracted 2D profiles at time t_3 ((b) and (d) respectively).

contour plots from the 2D reconstruction as in figure 11.

4. Evaluation of the mode displacement

The moment the 2D reconstruction has been performed, the evaluation of the mode displacement is relatively straightforward. If, as stated in the previous section, the electron temperature is still constant on the displaced flux surfaces, the shape of the T_e contours will coincide with that of the magnetic surfaces. In this case, an estimate of the maximum value of the mode displacement ξ (not of its radial profile) can be evaluated from the contour shapes.

The method is explained in figure 15a, where the T_e contours at t_3 are plotted for mode phase $\vartheta = 0$ as in the previous plots. The black rhombus in the centre of the figure is the original magnetic axis, while the red one is the centre of the displaced flux surface. The latter is evaluated as the average value of the LFS and HFS major radii of the most central contours (in red in figure):

$$R_{ax}^{new} = (R_{LFS} + R_{HFS})/2 \tag{15}$$

A total of 100 contour levels are used for this evaluation through the whole radial range. The maximum value of R_{ax}^{new} as evaluated through equation 15 is then taken for the calculation of the displacement ξ, equal to:

$$\xi = R_{ax}^{new} - R_{ax} \tag{16}$$

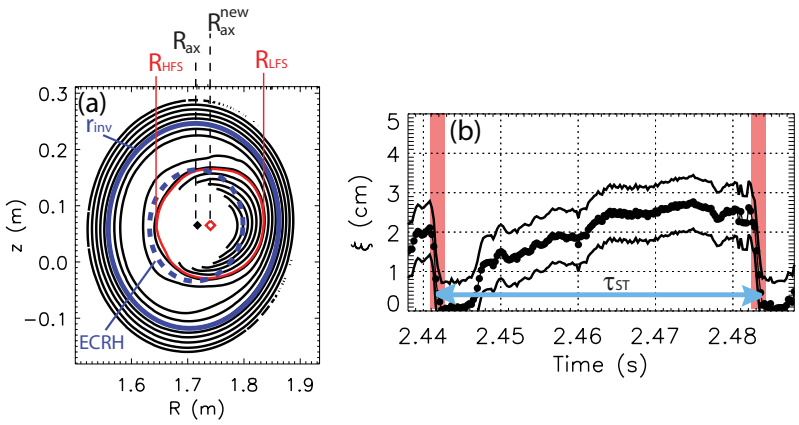

Figure 15. Geometric quantities used for the evaluation of the mode displacement as described in the text (a). Time evolution of the displacement (b); distance between upper and lower light black lines is the average distance between ECE channels inside the inversion radius. Shaded red areas show the region where the values cannot be trusted.

Calculating ξ for each time-point of the STFT, the time evolution of the mode displacement can be obtained. As shown in figure 15b, ξ goes to zero at the crashes (at $t \sim 2.443\ s$ and $t \sim 2.484\ s$) and reaches a maximum value of $\sim 3\ cm$. The upper and lower boundaries show the average distance (radial precision) of all the ECE channels inside the inversion radius and is therefore an upper limit for the error on the displacement. As explained in section 2.2, since the reconstruction of the 2D profiles fails at the crash time, the values of the displacement at these times (shaded red regions in figure 15b) are also not trustworthy.

Such an evaluation has been performed remapping on ϑ^* and the exact same values have been obtained. Instead, when using the $(1,1)$ component only, the displacement reaches values of $\sim 4\ cm$. This is consistent with those obtained using equation 8 in section 3.1 but is too high by $30-40$ % with respect to the more precise values obtained using all three components for the 2D reconstruction. When remapping on mode phase $\vartheta = \pi$, the displacement is instead $\sim 10\%$ higher due to the effect of the Shafranov shift.

5. Conclusions and outlook

A new method for the characterization of saturated MHD activity through the reconstruction of 2D electron temperature profiles from 1D ECE measurements has been presented. The method relies on the reconstruction of the measured data from its frequency components characterized through short time Fourier transform (STFT) and requires rigid poloidal rotation of the mode as only assumption. The high quality of the reconstruction method has been demonstrated through an example of an internal kink $(m,n) = (1,1)$ mode on ASDEX Upgrade. A new method for the evaluation of the internal kink displacement through a simple geometrical analysis of the 2D temperature contours has also been explained.

The two-dimensional reconstruction has revealed that the electron temperature

oscillation may exhibit higher harmonic components even for a pure $(m, n) = (1, 1)$ magnetic perturbation, explaining previous observations and modeling performed at TCV [19]. Since such higher harmonics are intrinsically due to the way the ECE measures the electron temperature perturbation, a one-to-one correspondence between higher order harmonics in the signal perturbation and harmonics in the magnetic perturbation cannot be done. Since also the magnetic coils and the SXR diagnostic cannot provide direct information on the higher harmonics, a possible way to characterize the MHD perturbation is to model its displacement vectors (m, n) including $m = n > 1$ harmonics, reconstruct the flux surfaces and search for a match with the contour plots from the 2D reconstruction provided in this paper.

Another consequence of this is that the evaluation of the displacement of a $(1, 1)$ mode from the 2D temperature reconstruction requires the use of all relevant harmonics in the electron temperature to correctly reconstruct the contours. The use of the first harmonic leads to values similar to those obtained using the formula $\xi = -\delta T_e / \nabla T_e$ [14], which is $30 - 40$ % higher than those evaluated using the new method. The reconstruction method is extendable to any magnetic perturbation as long as the poloidal and toroidal mode numbers m and n are known.

One of the possible future applications of the method is electron heat transport studies in the presence of saturated MHD activity (for any given (m, n) mode numbers) and of heat sources in and outside of the island structures. The results presented can also provide a way to disentangle impurity density contributions from electron temperature effects in the analysis of the SXR data. The emissivity profiles viewed by the SXR diagnostic are a convolution of these two effects and can be modeled as $\epsilon_A(R, z) = n_e(R, z)\, n_A(R, z)\, L_A\left(T_e(R, z)\right)$, where n_e is the electron density, n_A and L_A respectively the density and cooling factor of an impurity of mass A. In the core plasma, the latter is a mainly a function of electron temperature [20] and depends only slightly on transport. This method therefore provides a way of calculating mode-resolved 2D cooling factor profiles which can be used to calculate 2D impurity density profiles from the SXR data tomographic reconstructions.

A benchmarking against ECE-Imaging systems is also foreseen to investigate if the 2D reconstruction matches the measurements of the imaging system and to find out weather the mode behaves in the same way on both LFS and HFS of the magnetic axis.

Acknowledgments

Special thanks to Marc Maraschek and Emiliano Fable for the interesting and fruitful discussions. This work was partly funded by the European Commission under Association Contract between EURATOM and HAS. The views and opinions expressed herein do not necessarily reflect those of the European Commission.

References

[1] Kim J S *et al* 2001 *Plasma Physics and Controlled Fusion* **43** 1593
[2] Weiland M Simulation der Soft-X-Ray Diagnostic an ASDEX Upgrade in Anwesenheit von Plasmainstabilitäten und rotationsbedingten Strahlungsasymmetrien Technical report, IPP, Garching, Germany, September 2012 Diploma thesis LMU Munich, September 2012
[3] Hartfuss H J *et al* 1997 *Plasma Physics and Controlled Fusion* **39** 1693
[4] Munsat T *et al* Jul 2010 *Appl. Opt.* **49** E20–E30
[5] Yun G S *et al* 2010 *Review of Scientific Instruments* **81** 10D930

[6] Petravic G K 2-D time evolution of Te during sawtooth crash based on fast ECE measurements on TFTR Technical Report PPPL-2556, Princeton University, Plasma Physics Laboratory, 1988
[7] Nagayama Y *et al* 1990 *Review of Scientific Instruments* **61** 3265–3267
[8] Nicolas T *et al* 2012 *Physics of Plasmas* **19** 112305
[9] Mallat S *A Wavelet Tour of Signal Processing, Third Edition: The Sparse Way.* Academic Press, 2008
[10] Horváth L Short time Fourier transforms in NTI Wavelet Tools Technical Report 593, BME-NTI, Budapest, Hungary, November 2012
[11] Poli E *et al* 2001 *Computer Phys. Comm.* **136** 90–104
[12] Carthy P J M *et al* 2012 *Plasma Physics and Controlled Fusion* **54** 015010
[13] Schittenhelm M *et al* 1997 *Nuclear Fusion* **37** 1255–1270
[14] Fitzpatrick R 1995 *Physics of Plasmas* **2** 825–838
[15] Bussac M N *et al* Dec 1975 *Phys. Rev. Lett.* **35** 1638–1641
[16] Igochine V *et al* 2007 *Nuclear Fusion* **47** 23–32
[17] Wesson J *Tokamaks* Oxford Science Publications, 2011
[18] Mc Carthy P J Private communication, IPP Garching, 2012
[19] Furno I *et al* 2001 *Nucl. Fusion* **41** 403
[20] Sertoli M *et al* 2011 *Plasma Physics and Controlled Fusion* **53** 035024